Journal of
Materials Chemistry A

Materials for energy and sustainability

Accepted Manuscript

This article can be cited before page numbers have been issued, to do this please use: J. Xu, T. Li, Y. Zhang, E. J. Hansen, R. Godin and J. Liu, *J. Mater. Chem. A*, 2026, DOI: 10.1039/D6TA00814C.

ROYAL SOCIETY OF CHEMISTRY

rsc.li/materials-a

View Article Online
DOI: 10.1039/D6TA00814C

Atomic-Layer-Deposited Pd/Cu_2O/Cu Heterojunction as High-Efficiency Formate Catalysts and Boosting Aqueous Zn-CO_2 Batteries

Jia Xu, Li Tao, Yue Zhang, Evan J. Hansen, Robert Godin and Jian Liu**

J. Xu, L. Tao, Y. Zhang, E. J. Hansen, J. Liu
School of Engineering, Faculty of Applied Science, The University of British Columbia, Kelowna, British Columbia, V1V 1V7, Canada
R. Godin,
Department of Chemistry, The University of British Columbia, Kelowna, BC V1V 1V7, Canada
*Corresponding authors.
E-mail: jian.liu@ubc.ca; robert.godin@ubc.ca

View Article Online
DOI: 10.1039/D6TA00814C

The electrochemical reduction of carbon dioxide (CO_2RR) into value-added chemicals offers a sustainable pathway for mitigating greenhouse gas emissions and advancing carbon-neutral energy technologies. Among all possible CO_2RR products, formate/formic acid is particularly attractive due to its industrial relevance as a promising fuel for fuel cells and its high stability as an energy-storage medium. However, it remains challenging to obtain Cu-based catalysts with high selectivity and stability for CO_2 conversion to formate/formic acid. Herein, we report a metal Pd anchored onto a Cu_2O/Cu heterojunction (Pd–Cu_2O/Cu), synthesized via atomic layer deposition followed by electrochemical reduction. Structural and spectroscopic analyses confirmed that the presence of Pd atoms in the Cu_2O/Cu heterojunction collectively modulated the electronic states, stabilized *OCHO intermediates, suppressed the competing *H pathway, and balanced the *COOH pathway. Electrocatalytic tests of the Pd–Cu_2O/Cu in an H-type cell showed a remarkable formate Faradaic efficiency of 61.1% with a high partial current density of −24 mA cm^{-2} at −0.9 V versus RHE. When integrated into an aqueous Zn–CO_2 battery, the catalyst outperformed most reported Cu-based systems, achieving a maximum power density of 2.54 mW cm^{-2} and stable cycling for 130 hours. Overall, this work demonstrates a highly efficient Zn–CO_2 battery technology, highlighting the practical potential of coupling CO_2 utilization with sustainable energy storage.

Keywords: CO_2 electroreduction reaction, Cu_2O/Cu heterojunction, Formate, Pd catalyst, Zn-CO_2 battery

View Article Online
DOI: 10.1039/D6TA00814C

1. Introduction

The efficient electroreduction of carbon dioxide (CO_2) into value-added chemicals and fuels offers a promising approach to mitigate global warming and establish a sustainable, carbon-neutral energy cycle.[1, 2] Among various CO_2 reduction reaction (CO_2RR) pathways—such as C_1 products (CO, formate, CH_4, etc.),[3, 4] C_2 products (C_2H_4, CH_3CH_2OH, etc.),[5, 6] and C_3 products (n-propanol, etc.),[7, 8] the conversion of CO_2 to formate ($HCOO^-$)/formic acid (HCOOH) has emerged as one of the most promising routes, due to its substantial market potential as an industrial feedstock. In parallel, considering both the thermodynamic and kinetic energy barriers, the energy consumption for electroreduction of CO_2 to formic acid [$CO_2 + 2H^+ + 2e^- \rightarrow$ HCOOH, −0.19 V versus the reversible hydrogen electrode (RHE)] is relatively less than other products such as CH_3OH and CH_4. Therefore, designing catalysts that can selectively promote the formic acid reaction pathway has become a central focus in CO_2RR research.

Significant progress has been made in developing CO_2RR catalysts, including Pd, Pb, In, Sn, and Cu_2O, as well as their derivatives, which demonstrate enhanced electrocatalytic activity for formic acid production.[9-12] Cu-based catalysts have gained attention in CO_2RR due to the ease of processing and relatively low cost. For instance, Loiudice *et al*.[13] reported that Cu nanocubes exhibited a faradaic efficiency (FE) of 15% (at −1.1 V vs RHE) and a j_{HCOO-} ($HCOO^-$'s current density) value of ~1 mA cm^{-2} for formate. Despite these advances, Cu-based catalysts still suffer from insufficient selectivity toward formate due to their moderate binding energies with key intermediates. To address this challenge, strategies such as alloying, defect engineering, and single-atom dispersion have been proposed to fine-tune the catalytic sites and improve formate selectivity.[14, 15] Recently, Zeng et al.[16] regulated the first protonation step of the CO_2RR by building the single-atom Pb-alloyed Cu catalyst (Pb_1Cu), which improves to ~96% Faradaic efficiency of formate with high activity in excess of 1 A cm^{-2}.

Beyond elemental modification, the catalytic efficiency of Cu-based systems is also governed by particle size, structural reconstruction, and lattice facet exposure.[16, 17] Specific crystallographic orientations can direct product selectivity: the Cu(111) facet favors C_1 products such as CO and formate, while the Cu(110) and Cu(100) facets promote C_2 products including ethylene (C_2H_4).[18] In addition, oxide-derived Cu catalysts have been shown to significantly reduce the overpotential and enhance product selectivity compared with

View Article Online
DOI: 10.1039/D6TA00814C

conventional polycrystalline metallic Cu, owing to their unique surface defects and residual oxygen species. For example, Qiao *et al*.[19] developed a free-standing dendritic Cu heterojunction precatalyst (Cu_2O@Cu) via a facile electrochemical etching method, which underwent extensive structural reconstruction to form stepped Cu sites on a hierarchical dendritic array. The reconstructed Cu_2O@Cu exhibited up to ~50% formate selectivity at a low potential of –0.6 V (vs RHE). Similarly, Wang *et al.*[20] reported a Cu_2O/CuS composite catalyst that achieved an FE of 67.6% with a partial current density of 15.3 mA cm^{-2} at –0.9 V (vs RHE) for formate production, and maintained an average FE of 62.9% for at least 30 h under the same conditions, demonstrating both high activity and stability. Taken together, these examples illustrate the great potential of engineered Cu-based catalysts for formate production, while underscoring the ongoing challenge of achieving both high selectivity and long-term stability.

In parallel with the exploration of standalone CO_2RR electrocatalysts, researchers have sought to integrate CO_2 reduction into rechargeable battery systems, thereby coupling energy conversion with energy storage. Metal–CO_2 batteries, such as Li–CO_2 and Na–CO_2, have been widely investigated and have demonstrated high energy densities and improved cycling performance.[21] Nevertheless, the practical application of these systems has been limited by their reliance on toxic organic electrolytes, strict anhydrous and oxygen-free assembly conditions, accumulation of carbonaceous byproducts, and high operational costs. To overcome these drawbacks, aqueous Zn–CO_2 batteries (ZCBs) have been proposed as an attractive alternative. These systems not only provide energy output while consuming CO_2, but also enable the circular generation of valuable products such as CO, hydrocarbons, and HCOOH, which can be harvested as fuels and industrial feedstocks.[22] Despite these advantages, ZCBs remain relatively underexplored, with limited reported studies, all of which typically provide a discharge voltage below 0.5 V,[23-25] too low for widespread application. Therefore, further progress hinges on the rational design of cathode catalysts that can efficiently drive CO_2RR with high activity and selectivity, thereby enhancing the discharge voltage and narrowing the overall voltage gap.

Herein, we report a sustainable and reversible aqueous Zn–CO_2 battery employing a Pd-anchored Cu_2O/Cu heterojunction (Pd–Cu_2O/Cu) cathode paired with a Zn foil anode. The Pd–Cu_2O/Cu heterojunction was prepared by depositing Pd on Cu_2O nanocubes via atomic layer deposition (ALD) followed by electrochemical reduction, yielding Pd-modified Cu_2O/Cu

View Article Online
DOI: 10.1039/D6TA00814C

with increased surface area and enhanced catalytic activity. As a result, the Pd–Cu_2O/Cu achieved a high formate Faradaic efficiencies (FEs) of 61.1% and a large partial current density of −24 mA cm^{-2} at −0.9 V (vs RHE) in 0.5 M $KHCO_3$ within an H-type cell. When integrated into a Zn–CO_2 battery, the cathode delivered a maximum power density of 2.54 mW cm^{-2} and a high current density of 8.5 mA cm^{-2}, and a discharge potential of 0.65 V, maintaining stable operation for over 200 cycles (130 h). This work presents a highly efficient Zn–CO_2 battery platform with significant sustainability advantages, demonstrating the practical potential for direct CO_2 utilization in energy storage systems.

2. Results and Discussion

The synthesis strategy of the Pd–Cu_2O/Cu catalyst is shown in **Figure 1a**. The catalyst was fabricated through a modified wet-chemical reduction of a Cu_2O precursor, followed by atomic layer deposition (ALD) of Pd and the subsequent electrochemical reduction. In a typical wet-chemical reduction process, $CuCl_2$ aqueous solution and NaOH first reacted to form $Cu(OH)_2$, which was subsequently reduced to Cu_2O using ascorbic acid.[26] 100 ALD cycles of Pd was then deposited onto Cu_2O (denoted as Cu_2O@Pd-100) using $Pd(hfac)_2$ and plasma H_2 as precursors in a plasma-enhanced ALD system. The Pd content in Cu_2O@Pd-100 was determined to be 0.52 wt.% by inductively coupled plasma optical emission spectroscopy (ICP-OES). Prior to electrochemical measurements, the electrodes were reduced to form Pd–Cu_2O/Cu by electrochemical reduction for 5 mins in 0.5 M $KHCO_3$ at -0.5 V (vs RHE). The Cu_2O/Cu was obtained using Cu_2O precursor by the same electrochemical reduction process.

Scanning electron microscopy (SEM) and transmission electron microscopy (TEM) were employed to investigate the microstructure and lattice characteristics of the as-prepared Cu_2O, Cu_2O/Cu, and Pd–Cu_2O/Cu. As shown in **Figure 1b** and **Figure S1a**, pristine Cu_2O exhibited a well-defined cubic morphology with an average particle size of 200–300 nm. High-resolution TEM (HR-TEM) images of Cu_2O revealed lattice fringe spacings of 0.15 and 0.213 nm, corresponding to the (200) and (220) facets of Cu_2O (PDF #01-77-0199), respectively (**Figure S1b**). Raman spectra obtained from Cu_2O powder show four characteristic peaks at 148, 218, 415, and 625 cm^{-1} (**Figure S2**), assignable to Γ^-_{15}, $2\Gamma^-_{12}$, $4\Gamma^-_{15}$, and $\Gamma^-_{12}+\Gamma^-_{15}$ phonon modes of Cu_2O, respectively. [27] Together, these indicate the successful production of Cu_2O cubic structures suitable for ALD Pd coating in the next step.

View Article Online
DOI: 10.1039/D6TA00814C

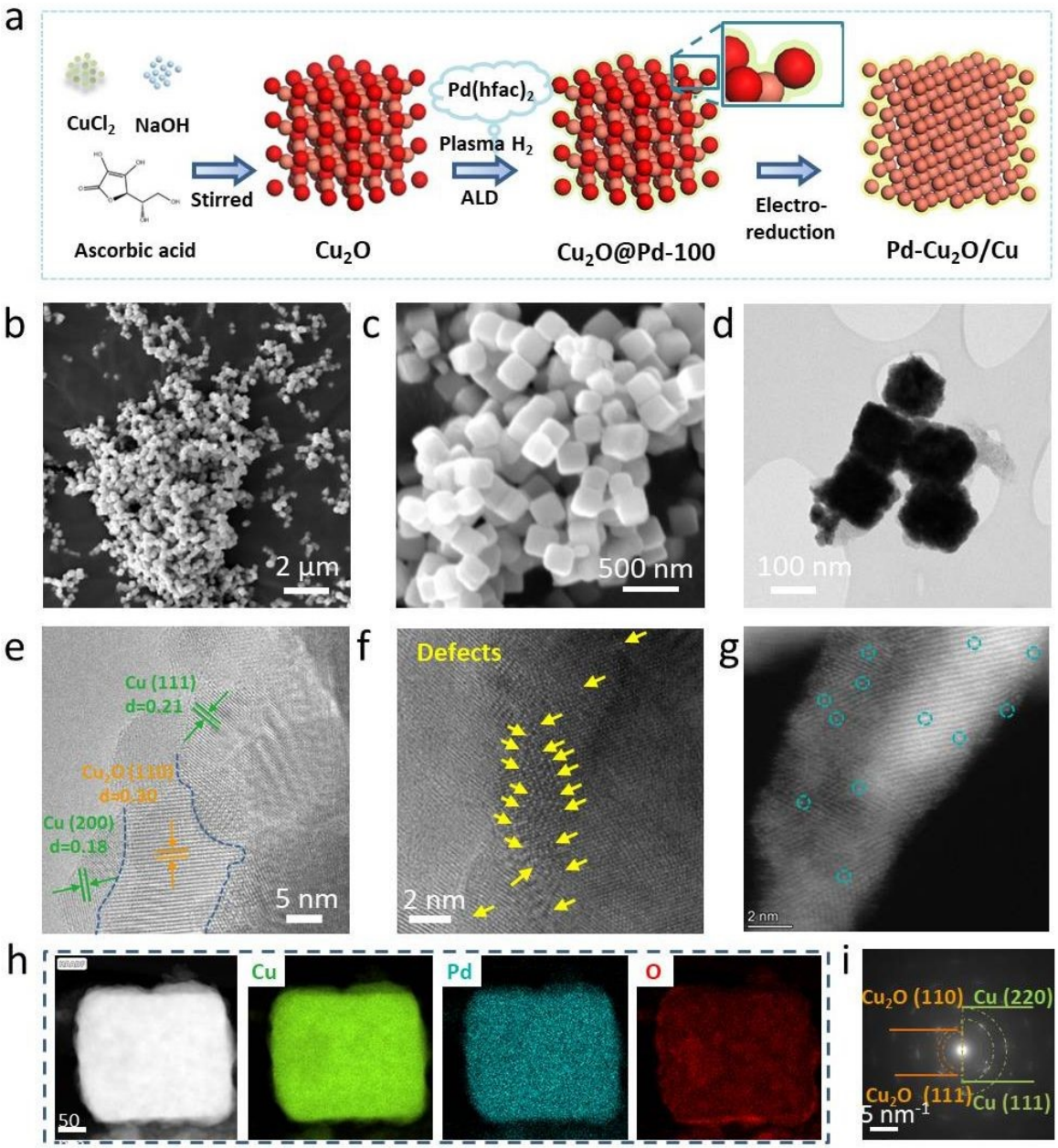

Figure 1 Synthesis route and physical characteristics of Pd–Cu_2O/Cu. (a) Schematic illustration of Pd–Cu_2O/Cu; SEM images of (b) Cu_2O, (c) Pd–Cu_2O/Cu; (d) TEM image of Cu_2O/Cu-Pd; (e, f) HR-TEM images of Pd–Cu_2O/Cu; (g) AC-HAADF-STEM image of Pd–Cu_2O/Cu; (h) HAADF-TEM image and corresponding elemental mapping of Pd–Cu_2O/Cu and (i) SAED pattern of Pd–Cu_2O/Cu.

Following ALD of Pd onto Cu_2O, SEM images of Pd-coated Cu_2O (Cu_2O@Pd-100) showed retention of the cubic Cu_2O morphology (**Figure S3**). After electrochemical reduction, the parent Cu_2O crystal facets were well-preserved, but with increased surface irregularity, as

View Article Online
DOI: 10.1039/D6TA00814C

seen in the SEM and TEM images of Pd–Cu_2O/Cu (**Figure 1c, d**). HR-TEM analysis revealed lattice fringes of 0.21, 0.18, and 0.30 nm, corresponding to the Cu (111), Cu (200), and Cu_2O (110) facets (Cu_2O PDF #01-77-0199; Cu PDF #00-004-0836), respectively (**Figure 1e**). The coexistence of lattice mismatch and abundant lattice defects in the Pd–Cu_2O/Cu catalyst was further confirmed by HR-TEM (**Figure 1f**). Furthermore, the atomic dispersion of Pd in Pd–Cu_2O/Cu was confirmed using aberration-corrected high-angle annular dark-field scanning transmission electron microscopy (AC-HAADF-STEM). The lighter dots, highlighted by blue circles in **Figure 1g**, were identified as Pd species. The high-angle annular dark field TEM (HAADF-TEM) image and corresponding elemental mapping (**Figure 1h**) demonstrated the uniform distribution of Cu and Pd throughout the Pd–Cu_2O/Cu. The selected area electron diffraction (SAED) pattern of Pd–Cu_2O/Cu (**Figure 1i**) displayed concentric diffraction rings indexed to Cu (220)/(111) and Cu_2O (110)/(111), corroborating the coexistence of Cu and Cu_2O phases after electroreduction. Similarly, the Cu_2O/Cu sample maintained its cubic morphology (**Figure S4a**). HR-TEM images of Cu_2O/Cu exhibited lattice spacings of 0.21 and 0.25 nm, consistent with the Cu (111) and Cu_2O (111) facets, respectively (**Figure S4b**).

The phase composition and surface chemical states of the catalysts were further investigated. In the XRD patterns of Cu_2O/Cu and Pd–Cu_2O/Cu (**Figure 2a**), diffraction peaks at 29.6°, 36.5°, 42.4°, and 61.5° correspond to the (110), (111), (200), and (220) planes of Cu_2O (PDF #01-77-0199), while the characteristic peaks at 44.4° and 54.6° are indexed to the (101) and (004) planes of carbon (PDF #00-023-0064) from the gas diffusion electrode (GDE). As shown in **Figure 2b**, new diffraction peaks at 43.3°, 50.4°, and 74.1° emerged in both Cu_2O/Cu and Pd–Cu_2O/Cu nanocubes, and correspond to the (111), (200), and (220) planes of metallic Cu (PDF #00-004-0836). The persistence of the Cu_2O (111) peak at 36.5° indicates that Cu_2O was only partially reduced to metallic Cu during the electrochemical reduction.

X-ray photoelectron spectroscopy (XPS) was performed to reveal the surface valence states and chemical bonding of Cu_2O/Cu and Pd–Cu_2O/Cu. In the Cu 2*p* spectra (**Figure 2c**), the peaks at 932.1 and 952.0 eV correspond to Cu $2p_{3/2}$ and Cu $2p_{1/2}$, respectively, consistent with Cu^0 or Cu^+ species.[28] The additional peaks at 934.2 and 954.4 eV, together with shake-up satellites near 942 eV, reveal the presence of Cu^{2+}, which is attributed to Cu(II) carbonate dihydroxide formed by air oxidation after electrochemical reduction in 0.5 M $KHCO_3$.[29] Cu LMM Auger electron spectroscopy (AES, **Figure 2d**) showed dominant peaks near 919.2 eV and 917.6 eV, characteristic of Cu^0 and Cu^+, further confirming the partial

View Article Online
DOI: 10.1039/D6TA00814C

reduction of Cu_2O to Cu_2O/Cu after electroreduction.[30] The O 1*s* spectrum displayed three distinct components: lattice oxygen (Cu–O, 530.5 eV), oxygen vacancies (O_v, 531.5 eV), and chemisorbed oxygen species (O_c, 532.8 eV). These results are consistent with the vacancy defects observed in HR-TEM (**Figure 2e**).[31] Notably, the content of oxygen vacancies in Pd–Cu_2O/Cu (47%) was higher than in Cu_2O/Cu (43%), calculated from the O 1*s* fitting XPS spectra. According to a previous report, the synergistic effect between facet-oriented Cu_2O and enriched oxygen vacancies has been proposed to facilitate CO_2 electroreduction to formate.[29] In the Pd 3*d* XPS spectrum of Pd–Cu_2O/Cu (**Figure 2f**), the peaks at 336.8 and 343.4 eV are assigned to the peak of Pd^{2+}.[32, 33] These findings confirm the absence of Pd nanoparticles and the successful formation of isolated Pd single atoms on the surface of the Pd–Cu_2O/Cu catalyst.

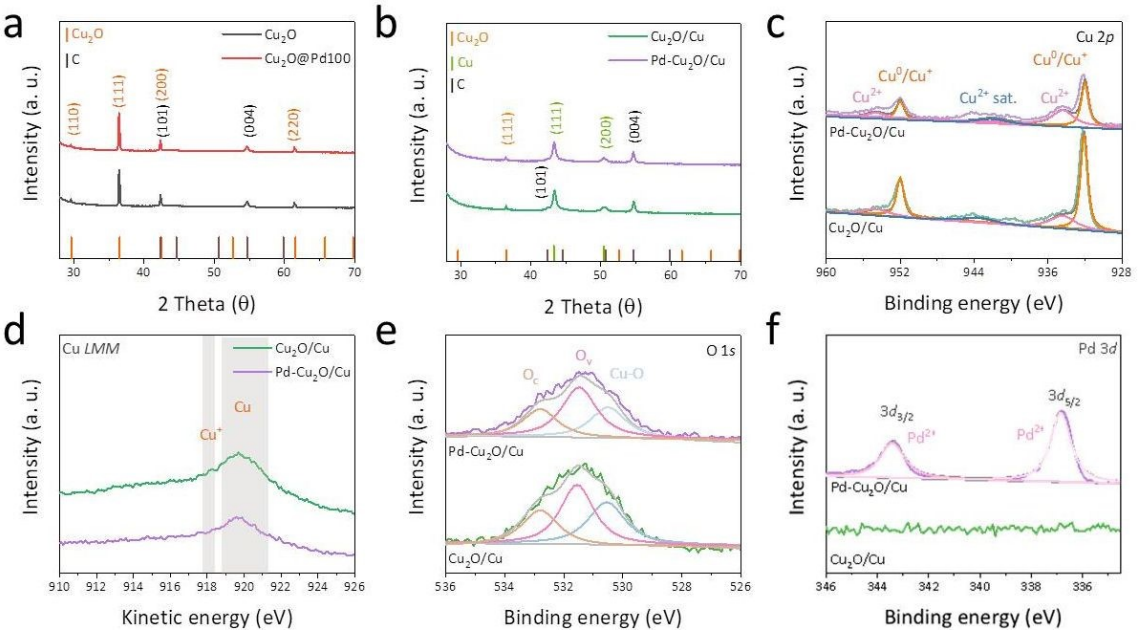

Figure 2 Physical and chemical characteristics of Cu_2O, Cu_2O@Pd100, and Pd–Cu_2O/Cu. (a) XRD pattern of Cu_2O and Cu_2O@Pd100; (b) XRD pattern of Cu_2O/Cu and Pd–Cu_2O/Cu; (c) Cu 2*p* XPS spectra of Cu_2O/Cu and Pd–Cu_2O/Cu; (d) Cu *LMM* Auger spectra of Cu_2O/Cu and Pd–Cu_2O/Cu; (e) O 1*s* and (f) Pd 3*d* XPS spectra of Cu_2O/Cu and Pd–Cu_2O/Cu.

We studied the CO_2RR properties of the GDE-supported Cu_2O/Cu and Pd–Cu_2O/Cu catalysts (active GDE area, 1 cm^2; catalyst loading, 0.5 mg cm^{-2}) in an H-cell setup with a CO_2- and N_2-saturated 0.5 M $KHCO_3$ electrolyte. All data was recorded after electrochemical

View Article Online
DOI: 10.1039/D6TA00814C

reduction and 20 cycles of potential scans over the range of 0 to -0.4 V (vs RHE) at a scan rate of 20 mV s^{-1}, to reduce Cu_2O to Cu^0 and a small quantity of metastable Cu^+. Linear sweep voltammetry (LSV) measurements were performed in the electrolyte at a scan rate of 10 mV s^{-1} both in the N_2- and CO_2-saturated 0.5 M $KHCO_3$ aqueous solutions. As shown in **Figure 2a**, the onset potential of two catalysts in CO_2-saturated $KHCO_3$ solution both shifted to the positive direction compared with that in the N_2-saturated $KHCO_3$ solution. In the CO_2-saturated 0.5 M $KHCO_3$ aqueous solutions, Pd–Cu_2O/Cu provides a more positive onset potential (-0.49 V vs RHE at j=10 mA cm^{-2}) than that of Cu_2O/Cu (-0.58 V vs RHE at j=10 mA cm^{-2}). The current density of the Pd–Cu_2O/Cu catalyst increased rapidly as the potential became increasingly negative and reached approximately 32 and 43 mA cm^{-2} at -0.9 and -1.1 V (vs RHE), respectively. In **Figures 3b and c**, the electrochemical surface area (ECSA) of the as-obtained samples is evaluated using the double-layer capacitance (C_{dl}) method. Pd–Cu_2O/Cu catalyst exhibited a C_{dl} value of 10.06 mF cm^{-2} (**Figure 3d**), which is almost double that of Cu_2O/Cu (5.83 mF cm^{-2}), indicating a greater exposure of active sites in Pd–Cu_2O/Cu. In **Figure S5**, the Tafel slope of Pd–Cu_2O/Cu (412 mV dec^{-1}) is higher than that of Cu_2O/Cu (505 mV dec^{-1}), implying Pd–Cu_2O/Cu has a high reaction rate, which was significantly improved by CO_2 activation.

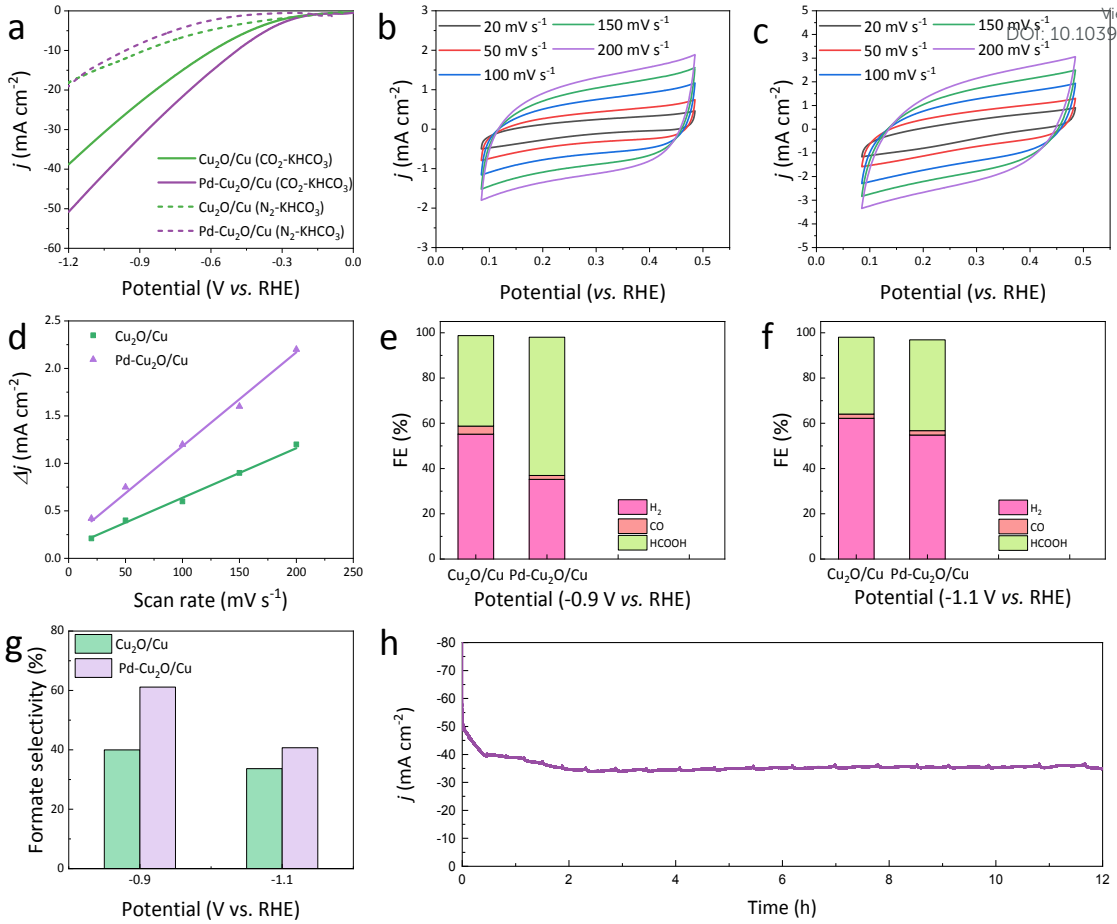

Figure 3 CO_2RR performance of Cu_2O/Cu and Pd–Cu_2O/Cu. (a) LSV curves of Cu_2O/Cu and Pd–Cu_2O/Cu in a H-type cell with CO_2-saturated and N_2-saturated. CV curves measured at 20, 50, 100, 150 and 200 mV s^{-1} in a H-type cell; (b): Cu_2O/Cu and (c): Pd–Cu_2O/Cu; (d) The C_{dl} values of Cu_2O/Cu and Pd–Cu_2O/Cu. Product distribution of Cu_2O/Cu and Pd–Cu_2O/Cu at (e) -0.9 V (vs RHE) and (f) -1.1 V (vs RHE), (g) Comparison of $FE_{formate}$ for Cu_2O/Cu and Pd–Cu_2O/Cu catalysts. (h) Stability test of Pd–Cu_2O/Cu at -0.9 V (vs RHE).

The distribution of gaseous (i.e., CO, CH_4, and C_2H_2) and liquid products (i.e., formate ($HCOO^-$), ethane-diol ($CH_3CH(OH)_2$), acetic acid (CH_3COOH), and acetaldehyde (CH_3CHO)) obtained during the CO_2RR process was assessed using gas chromatography (GC) and *ex-situ* Nuclear Magnetic Resonance (NMR) in 0.5 M $KHCO_3$ electrolyte. **Figures 3e and f** present the obtained Faradaic efficiencies (FEs) of products with Cu_2O/Cu and Pd–Cu_2O/Cu at -0.9 and -1.1 V (vs RHE), respectively. As the applied potential varied, the Cu_2O/Cu catalyst became more negative, FE for formate from about 48.2% to 40.1% under -0.9 and -1.1 V (vs RHE) with a slight increase in H_2. The FE for formate production with different catalysts is

View Article Online
DOI: 10.1039/D6TA00814C

compared in **Figure 3g**. Compared with Cu_2O/Cu, the FE for formate on Pd–Cu_2O/Cu increases, reaching 61.1% at -0.9 V (vs RHE). The improvement may result from the structural reconstruction of the catalyst and a synergistic effect between Pd modification and the catalytically active Cu sites during CO_2RR.[19, 34, 35] As the applied potential becomes increasingly negative, the FE for formate decreases and remains over 40 % when the potential is more negative than -1.1 V (vs RHE), whereas that for H_2 increases to 54.8 %. The chronoamperometry (CA) curves and *ex-situ* ^{1}H NMR spectra are shown in **Figures S6 and S7**. Although Cu_2O or Cu catalysts have been reported to promote the formation of C_2H_4 during the CO_2 reduction reaction, the generation of C_{2+} products typically requires highly negative potentials under alkaline conditions, where the elevated pH can lower the C–C coupling energy barrier while simultaneously suppressing competing reactions such as H_2 and CH_4 evolution.[36, 37] In published reports, Cu-derived heterojunction electrocatalysts have been shown to produce liquid products, particularly formate.[38, 39] The Pd–Cu_2O/Cu catalyst favors the production of formic acid, probably due to the incorporation of Pd, which enhances interfacial charge redistribution within the catalyst and modulates its *d*-band electronic structure.[40] Furthermore, during continuous electrocatalysis at -0.9 V (vs. RHE) (**Figure 3h**), Pd–Cu_2O/Cu maintains a high stability with minimal potential degradation for 12 h, which was better than most reported Cu-based electrocatalysts, as summarized in **Table S1**. As shown in **Figure S8**, after stability test for 12 h, the FE for formate decreased from 61.1% to 54.2 %, and FE retention achieved to 88.7%. The typical cubic morphology of Pd–Cu_2O/Cu had been retained after the long-term electrolysis (**Figure S9**). This indicated the superiority of the Pd–Cu_2O/Cu constructed for activity and selectivity for formic acid.

View Article Online
DOI: 10.1039/D6TA00814C

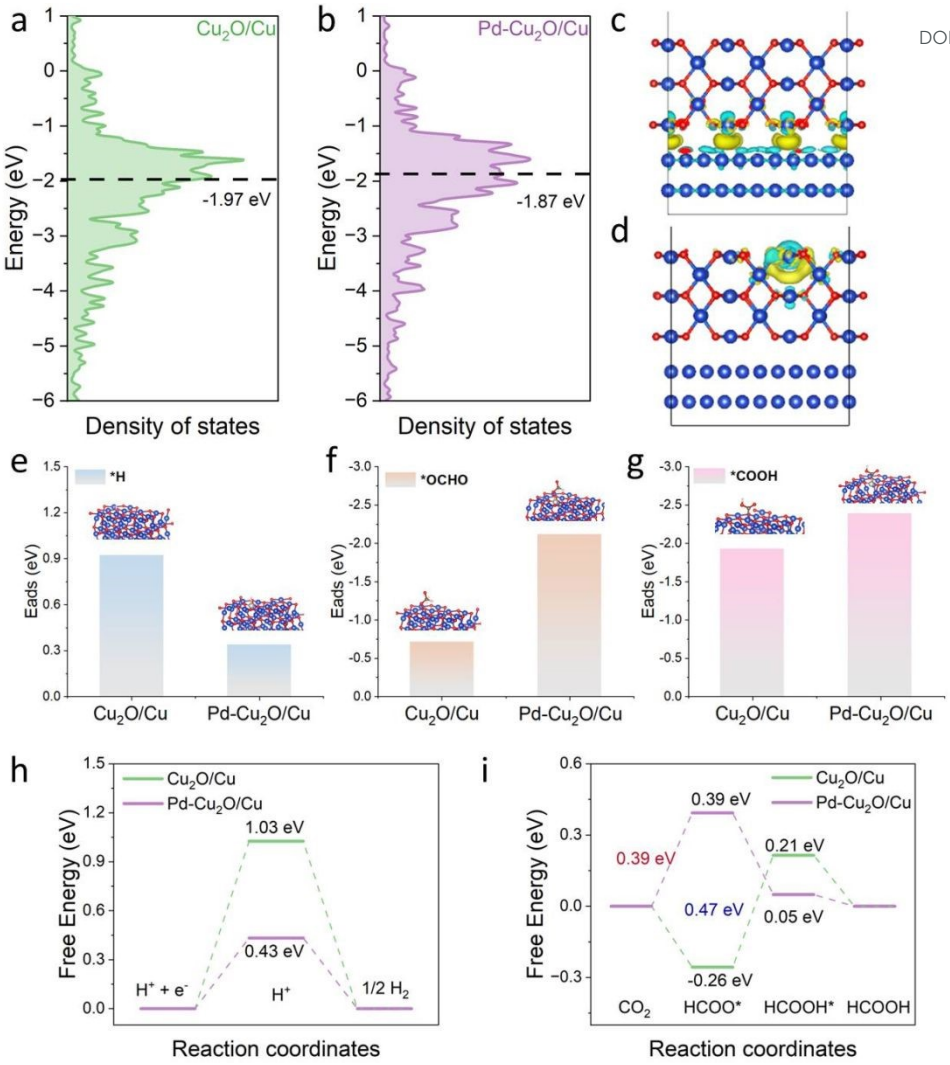

Figure 4 Theoretical calculations. PDOS of Cu 3*d* orbitals for (a) Cu_2O/Cu and (b) Pd–Cu_2O/Cu; differential charge density and Bader charge simulations of (c) Cu_2O/Cu and (d) Pd–Cu_2O/Cu; the calculated adsorption energy of (e) *H, (f) *OCHO and (g) *COOH on Cu_2O/Cu and Pd–Cu_2O/Cu, respectively; the free energy diagram of producing (h) H_2 and (i) formic acid on Cu_2O/Cu and Pd–Cu_2O/Cu, respectively.

To gain further insights into the underlying mechanisms, density functional theory (DFT) calculations were employed. The optimized models of Cu_2O/Cu and Pd–Cu_2O/Cu are constructed in **Figure S10**. As depicted in **Figure 4a, b**, the partial density of state (PDOS) analyses for Cu 3*d* orbitals revealed that Pd–Cu_2O/Cu had an elevated *d*-band center −1.87 eV, being closer to the Fermi level than that of the Cu site in Cu_2O/Cu. The higher *d*-band center of the Cu led to reinforced adsorption behaviors of Pd–Cu_2O/Cu surface.[41, 42] The differential charge density and Bader charge were simulated (**Figure 4c, d and Figure S11**). The positive Δρ (yellow) and negative Δρ (blue) represent electron accumulation and

View Article Online
DOI: 10.1039/D6TA00814C

depletion regions, respectively. Bader charge of Pd–Cu_2O/Cu is higher than Cu_2O/Cu, in which the Pd stom doping on Pd–Cu_2O/Cu promotes electron transfer from Pd–Cu_2O/Cu surface to the intermediates, leading to high-density electron depletion regions on the Pd side and indicating a strong electronic interaction with the adsorbates. During the CO_2RR process, the active sites and electrons on the surface might be occupied and consumed by intermediates of multiple reactions, leading to a decline in the catalytic efficiency of CO_2RR. Hence, the adsorption energy of *H, *OCHO and *COOH on the different catalyst surface was calculated. As shown in **Figure 4e-g and Figures S12-13**. The adsorption energy of *H on the Pd–Cu_2O/Cu is 0.33 eV more than 0 eV (**Figure 4e**), and lower than that of Cu_2O/Cu, suggesting that Pd atoms doping is beneficial for effectively restraining the HER through a stronger interaction with adsorbed *H. In **Figure 4f**, the adsorption energy of *OCHO intermediates on the Pd–Cu_2O/Cu is -2.12 eV, lower than that of Cu_2O/Cu (-0.71 eV), implying that Pd–Cu_2O/Cu could effectively promote the selectivity of formate through stronger interaction with adsorbed *OCHO intermediates. In addition, considering the intermediate to produce CO, the adsorption energy of *COOH intermediate on the Pd–Cu_2O/Cu is -2.39 eV, lower than that of Cu_2O/Cu (-1.93 eV), suggesting that Pd–Cu_2O/Cu could effectively enhance the efficiency of CO (**Figure 4g**). In other words, the Pd–Cu_2O/Cu catalyst enhances the adsorption process of *OCHO and *COOH intermediates. It could be contradictory that the Pd–Cu_2O/Cu could increase the efficiency of formate as same as CO in thermodynamical process. **Figure 4i** displays the Gibbs free energy profiles during the CO_2RR on the surface of Pd-Cu_2O/Cu, accompanied by the profiles for Cu_2O/Cu for purposes of comparison. The ΔG value associated with the rate-determining step (RDS) is positive and highest throughout the entire CO_2RR process.[43, 44] Notably, the transition from CO_2 to *OCHO, from *OCHO to *HCOOH represents the RDS for Pd–Cu_2O/Cu and Cu_2O/Cu during the CO_2RR, respectively. It is evident that the reaction free energy for the RDS is lower on Pd–Cu_2O/Cu (0.39 eV) compared to Cu_2O/Cu (0.47 eV). This suggests that the incorporation of Pd atoms into Cu_2O/Cu reduces the reaction energy barrier of the RDS, thereby facilitating the formate production process during CO_2RR. Moreover, the ΔG *H on Pd–Cu_2O/Cu is 0.43 eV, which is lower than that of Cu_2O/Cu (1.03 eV), but more than 0 eV, confirming that Pd–Cu_2O/Cu significantly suppresses its competing HER across a broad potential window to optimal the CO_2RR process. Although * COOH is thermodynamically more stable (-2.39 eV), due to the energy barrier from CO_2 to *OCHO being only 0.39 eV and the rapid conversion of

View Article Online
DOI: 10.1039/D6TA00814C

*OCHO to HCOOH, the reaction kinetics effectively bypass the *COOH pathway, thereby avoiding competition from the CO pathway. Thus, combining theoretical and experimental analyses, it is strongly supported that the inhibition of parallel reactions on Pd–Cu_2O/Cu surface plays a crucial role in achieving efficient CO_2 reduction to formate.

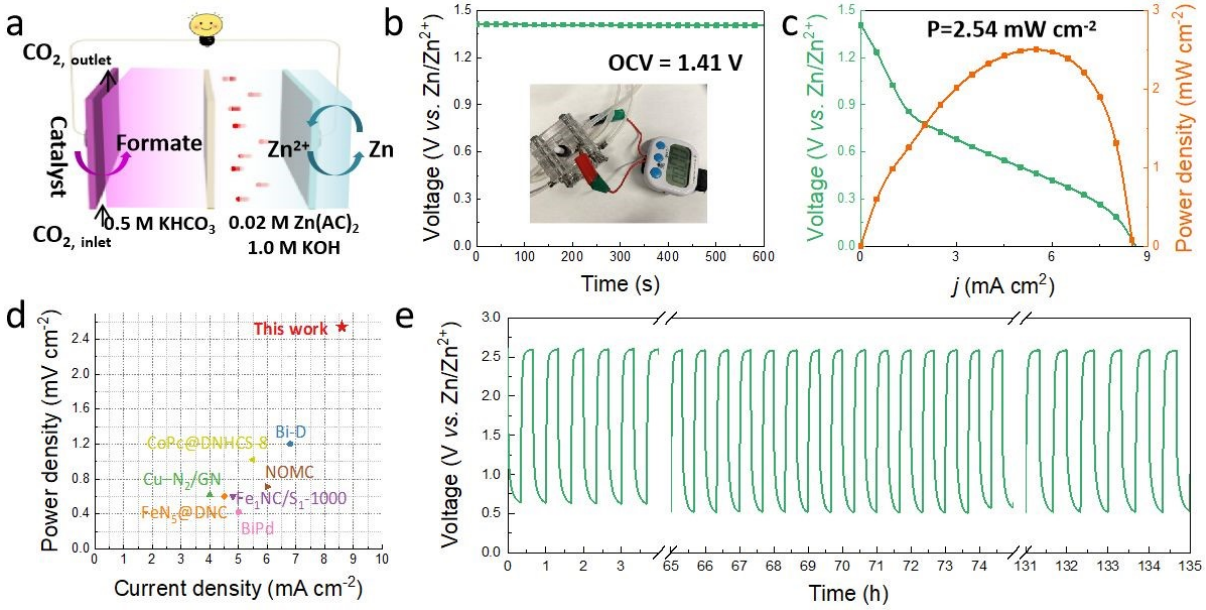

Figure 5 The electrochemical performance of Zn-CO_2 battery (ZCBs). (a) Schematic illustration of the designed ZCBs with Pd–Cu_2O/Cu as the cathode; (b) open circuit voltage over time with an inst showing the digital photo of an electronic timer powered by one ZCB; (c) discharge curves and power density; (d) comparison of the obtained current and power density of our work to others, and (e) galvanostatic discharge–charge cycling curves at 0.5 mA cm^{-2}.

Given the excellent catalytic performance of Pd–Cu_2O/Cu toward CO_2RR, a Zn–CO_2 battery (ZCB) was further investigated as a promising energy conversion system for CO_2 utilization. The Zn–CO_2 battery was assembled in a flow cell with a GDE, and the Pd–Cu_2O/Cu catalyst and a Zn plate were applied as the cathode and anode, respectively. The cell configuration and the working principle of a Zn–CO_2 battery are schematically illustrated in **Figure 5a**. During discharge, Zn is oxidized to Zn^{2+} at the anode with the release of electrons, while CO_2 reduction occurs at the cathode. Conversely, during charging, Zn^{2+} at the anode is reduced back to metallic Zn, accompanied by the oxygen evolution reaction (OER) at the cathode. As shown in **Figure 5b**, the open-circuit voltage (OCV) of the ZCB was 1.41 V and remained

View Article Online
DOI: 10.1039/D6TA00814C

stable for 10 min. The discharge polarization and corresponding power density curves are presented in **Figure 5c and Figure S14**. The peak power density of the ZCB with Pd–Cu_2O/Cu cathode was determined to be 2.54 mW cm^{-2} at a high current density of 8.5 mA cm^{-2}, which was much higher than that for the Cu_2O/Cu (1.32 mW cm^{-2}) cathodic catalyst, outperforming several recently reported catalysts (**Figure 5d** and **Table S2**).[45-53] Furthermore, at discharge current densities of 0.5, 1.0, 2.0, and 3.0 mA cm^{-2}, the ZCB employing the Pd–Cu_2O/Cu cathode exhibited stable voltage plateaus of approximately 1.17, 1.07, 0.78, and 0.62 V, respectively, over a period of one hour. When the discharge current density was reduced to 0.5 mA cm^{-2}, the stable voltage plateau of the ZCB with the Pd–Cu_2O/Cu cathode reached approximately 1.21 V, indicating favorable discharge characteristics of this battery (**Figure S15**). At a constant current density of 0.5 mA cm^{-2} (**Figure 5e and Figure S16**), the charge-discharge cycles and corresponding discharge efficiency of ZCB with Pd–Cu_2O/Cu cathode were each set to 20 mins (total 40 mins per cycle). The ZCB device exhibits a charge potential of 2.62 V and a discharge potential of 0.65 V, while delivering excellent cycling stability for over 200 cycles and maintaining robust operational performance for 135 h without noticeable degradation. No significant change in the typical morphology or composition of Pd–Cu_2O/Cu was observed after the long-term cycling of the ZCB (**Figure S17**), indicating favorable structural stability of the Pd–Cu_2O/Cu catalyst. Furthermore, as shown in the inset of **Figure 5b**, a single aqueous rechargeable ZCB employing the Pd–Cu_2O/Cu cathode successfully powered an electronic timer, suggesting the practicability of this aqueous Zn–CO_2 battery.

3. Conclusion

We developed a Pd anchored on a Cu_2O/Cu heterojunction (Pd–Cu_2O/Cu), which exhibited outstanding activity and selectivity for CO_2 electroreduction. It was found that the introduction of Pd induced electron localization and lattice strain at the Cu_2O/Cu interface, favoring the stabilization of key intermediates (e.g., *OCHO) while suppressing competitive *H and *COOH adsorption pathways. As a result, the Pd–Cu_2O/Cu catalyst achieved a high Faradaic efficiency for CO_2 reduction to formate of 61.1% at −0.9 V (vs RHE), along with a large partial current density of −24 mA cm^{-2} in H-type cell tests. When integrated into an aqueous Zn–CO_2 battery, Pd–Cu_2O/Cu delivered superior performance with an ultralow loading of 0.5 mg cm^{-2}, sustaining high current (8.5 mA cm^{-2}), power densities (2.54 mW cm^{-}

View Article Online
DOI: 10.1039/D6TA00814C

^{2}), and discharge voltage (0.65 V)under continuous CO_2 purging–values, surpassing the performance of most reported catalysts. This work not only demonstrates a highly efficient route to valorize excess atmospheric CO_2, but also establishes a sustainable pathway toward advanced energy-storage devices that couple CO_2 utilization with renewable energy integration, simultaneously mitigating CO_2 emissions and advancing electrification.

Author contributions

Jia Xu: writing-original draft, synthesis, methodology, investigation, formal analysis, data curation, conceptualization. Li Tao, Yue Zhang and Evan J. Hansen: validation, writing-review & editing, methodology, investigation. Robert Godin: writing-review & editing, supervision, validation, investigation. Jian Liu: writing-review & editing, supervision, project administration, funding acquisition.

Acknowledgments

This research was supported by the Natural Sciences and Engineering Research Council of Canada (NSERC), Canada Foundation for Innovation (CFI), BC Knowledge Development Fund (BCKDF), the University of British Columbia (UBC), and UBC Eminence Program (Net Zero Research Excellence Cluster and Battery Innovation Research Excellence Cluster). The authors are grateful to Dr. Carmen Andrei for HRTEM characterizations at the Canadian Centre for Electron Microscopy (CCEM) at McMaster University, and Dr. Shihong Xu and Dr. Peng Li for XPS characterizations at NanoFAB at the University of Alberta.

References

[1] S. Hao; A. Elgazzar; S. K. Zhang; T. U. Wi; F. Y. Chen; Y. Feng; P. Zhu; H. Wang, *Science* ***288***, 1182.

[2] W. Ma; J. Morales-Vidal; J. Tian; M. T. Liu; S. Jin; W. Ren; J. Taubmann; C. Chatzichristodoulou; J. Luterbacher; H. M. Chen; N. López; X. Hu, *Nature* 2025, ***641***, 1156-1161.

[3] W. Zhang; A. Mehmood; G. Ali; H. Liu; L. Chai; J. Wu; M. Liu, *Angew. Chem., Int. Ed.* 2025, ***64***, e202424552.

[4] C. Wang; Z. Lv; Y. Liu; R. Liu; C. Sun; J. Wang; L. Li; X. Liu; X. Feng; W. Yang; B. Wang, *Angew. Chem., Int. Ed.* 2024, ***63***, e202404015.

[5] D. Zhou; C. Chen; Y. Zhang; M. Wang; S. Han; X. Dong; T. Yao; S. Jia; M. He; H. Wu; B. Han, *Angew. Chem., Int. Ed.* 2024, ***63***, e202400439.

[6] W. Choi; Y. Chae; E. Liu; D. Kim; W. S. Drisdell; H. S. Oh; J. H. Koh; D. K. Lee; U. Lee; D. H. Won, *Nat. Commun.* 2024, ***15***, 8345.

[7] M. Choi; S. Bae; Y. Kim; Y. Lee; M. Cho; S. Kang; J. Lee, *Nat. Catal.* 2025, ***8***, 476-486.

[8] K. Qi; Y. Zhang; N. Onofrio; E. Petit; X. Cui; J. Ma; J. Fan; H. Wu; W. Wang; J. Li; J. Liu; Y. Zhang; Y. Wang; G. Jia; J. Wu; L. Lajaunie; C. Salameh; D. Voiry, *Nat. Catal.* 2023, ***6***, 319-331.

[9] Y. Wei; X. Wang; J. Mao; Y. Song; H. Zhu; X. Liu; C. Luo; S. Li; A. Chen; G. Li; X. Dong; W. Wei; W. Chen, *Angew. Chem. Int. Ed.* 2025, ***137***, e202423370.

[10] Y. Shi; Y. Ji; J. Long; Y. Liang; Y. Liu; Y. Yu; J. Xiao; B. Zhang, *Nat. Commun.* 2020, ***11***, 3415.

[11] B. Jia; Z. Chen; C. Li; Z. Li; X. Zhou; T. Wang; W. Yang; L. Sun; B. Zhang, *J. Am. Chem. Soc.* 2023, ***145***, 14101-14111.

[12] M. Wang; J. Jia; J. Xia; C. K. Peng; J. He; Y. Qiu; Y. He; L. Gao; F. Xue; Y. G. Lin; G. Zhan; Y. Guo; X. Huang; Y. Xu, *Nat. Commun.* 2025, ***16***, 6454.

[13] A. Loiudice; P. Lobaccaro; E. A. Kamali; T. Thao; B. H. Huang; J. W. Ager; R. Buonsanti, *Angew. Chem., Int. Ed.* 2016, ***55***, 5613-5868.

[14] S. Nitopi; E. Bertheussen; S. B. Scott; X. Liu; A. K. Engstfeld; S. Horch; B. Seger; I. E. L. Stephens; K. Chan; C. Hahn; J. K. Norskov; T. F. Jaramillo; I. Chorkendorff, *Chem Rev* 2019, ***119***, 7610-7672.

[15] J. Dong; Y. Liu; J. Pei; H. Li; S. Ji; L. Shi; Y. Zhang; C. Li; C. Tang; J. Liao; S. Xu; H. Zhang; Q. Li; S. Zhao, *Nat. Commun.* 2023, ***14***, 6849.

[16] T. Zheng; C. Liu; C. Guo; M. Zhang; X. Li; Q. Jiang; W. Xue; H. Li; A. Li; C. W. Pao; J. Xiao; C. Xia; J. Zeng, *Nat Nanotechnol* 2021, ***16***, 1386-1393.

[17] S. Liang; J. Xiao; T. Zhang; Y. Zheng; Q. Wang; B. Liu, *Angew. Chem. Int. Ed.* 2023, ***135***, e202310740.

[18] Z. Z. Wu; X. L. Zhang; Z. Z. Niu; F. Y. Gao; P. P. Yang; L. P. Chi; L. Shi; W. S. Wei; R. Liu; Z. Chen; S. Hu; X. Zheng; M. R. Gao, *J. Am. Chem. Soc.* 2022, ***144***, 259-269.

[19] S. Qiao; G. Zhang; D. Tian; W. Xu; W. Jiang; Y. Cao; J. Qian; J. Zhang; Q. He; L. Song, *Energy Environ. Sci.* 2024, ***17***, 6779-6786.

[20] S. Wang; T. Kou; J. B. Varley; S. A. Akhade; S. E. Weitzner; S. E. Baker; E. B. Duoss; Y. Li, *ACS Materials Letters* 2020, ***3***, 100-109.

[21] X. Zhang; N. Zhao; H. Zhang; Y. Fan; F. Jin; C. Li; Y. Sun; J. Wang; M. Chen; X. Hu, *Nanomicro Lett* 2024, ***17***, 99.

[22] J. Xu; M. Galib; Z. Wu; L. Tao; Y. Shao; Y. Zhang; X. Guo; E. J. Hansen; Y. Chen; Z. Wang; C. Liu; M. Ponga; J. Liu, *Nano Energy* 2024, ***132***, 110373.

[23] Z. Zeng; L. Y. Gan; H. Bin Yang; X. Su; J. Gao; W. Liu; H. Matsumoto; J. Gong; J. Zhang; W. Cai; Z. Zhang; Y. Yan; B. Liu; P. Chen, *Nat. Commun.* 2021, ***12***, 4088.

[24] L. L. Ling; L. Jiao; X. Liu; Y. Dong; W. Yang; H. Zhang; B. Ye; J. Chen; H. L. Jiang, *Adv. Mater.* 2022, ***34***, e2205933.

[25] J. Chen; Z. Li; X. Wang; X. Sang; S. Zheng; S. Liu; B. Yang; Q. Zhang; L. Lei; L. Dai; Y. Hou, *Angew. Chem., Int. Ed.* 2021, ***61***, e202111683.

[26] D.-F. Zhang; H. Zhang; L. Guo; K. Zheng; X.-D. Han; Z. Zhang, *Journal of Materials Chemistry* 2009, ***19***, 5220.

[27] K. Zhang; B. Li; F. Guo; N. Graham; W. He; W. Yu, *Angew. Chem., Int. Ed.* 2024, e202411796.

[28] L. Wan; Q. Zhou; X. Wang; T. E. Wood; L. Wang; P. N. Duchesne; J. Guo; X. Yan; M. Xia; Y. F. Li; F. M. Ali; U. Ulmer; J. Jia; T. Li; W. Sun; G. A. Ozin, *Nat. Catal.* 2019, ***2***, 889-898.

[29] G. Li; Y. Song; C. Zhu; X. Dong; W. Chen; G. Wu; G. Feng; S. Li; W. Wei, *Journal of CO2 Utilization* 2023, ***70***, 102446.

[30] Y. Gao; S. Yu; P. Zhou; X. Ren; Z. Wang; Z. Zheng; P. Wang; H. Cheng; Y. Liu; W. Wei; Y. Dai; B. Huang, *Small* 2022, ***18***, e2105212.

[31] J. Fu; F. M. Hassan; C. Zhong; J. Lu; H. Liu; A. Yu; Z. Chen, *Adv. Mater.* 2017, ***29***, 1702526.

[32] Q. Wei; C. Yu; X. Song; Y. Zhong; L. Ni; Y. Ren; W. Guo; J. Yu; J. Qiu, *J. Am. Chem. Soc.* 2021, ***143***, 6071-6078.

[33] G. Li; X. Wang; L. Yan; Y. Wang; Z. Zhang; J. Xu, *ACS Appl. Mater. Interfaces* 2019, ***11***, 26116-26126.

[34] R. Zhou; X. Fan; X. Ke; J. Xu; X. Zhao; L. Jia; B. Pan; N. Han; L. Li; X. Liu; J. Luo; H. Lin; Y. Li, *Nano Lett* 2021, ***21***, 4092-4098.

[35] J. Li; S. X. Guo; F. Li; F. Li; X. Zhang; J. Ma; D. R. MacFarlane; A. M. Bond; J. Zhang, *ChemSusChem* 2019, ***12***, 4471-4479.

[36] C. Lu; Q. He; S. Huang; P. Shi; C. Yang; J. Zhang; J. Zhu; J. Zhang; TianfuWang; X. Zhuang, *Adv. Mater.* 2025, ***37***, e2415092.

[37] S. Chen; C. Ye; Z. Wang; P. Li; W. Jiang; Z. Zhuang; J. Zhu; X. Zheng; S. Zaman; H. Qu; L. Lv; L. Tan; Y. Su; J. Ouyang; D. Wang, *Angew. Chem., Int. Ed.* 2023, ***62***, e202315621.

[38] S. Wu; S. Li; Z. Hou; Y. Hu; Z. Zhang; J. Zhu; S. Xu; R. Wang; N. Zhang; L. An; P. Xi; C. H. Yan, *Adv. Mater.* 2025, ***37***, e2503772.

[39] Y. Shi; Y. Wang; J. Yu; Y. Chen; C. Fang; D. Jiang; Q. Zhang; L. Gu; X. Yu; X. Li; H. Liu; W. Zhou, *Adv. Energy Mater.* 2023, ***13***, 2203506.

[40] X. Zhang; L. Hui; F. He; Y. Li, *J. Am. Chem. Soc.* 2025, ***147***, 436-445.

[41] F. Wang; H. Tian; B. Nan; G. Chen; K. Song; S. Wang; S. Chen; S. Yin; Z. Lu; W. Tu; W. Jiang; S. Wang; G. Liu, *J. Am. Chem. Soc.* 2026.

[42] P. Chen; X. Liu; D. He; Y. Liao; H. Li; J. Cheng; Y. Lu; Z. Yang; Y. Yang; F. Jin, *Nat. Commun.* 2026, ***17***, 2395.

[43] H. G. Qin; Y. F. Du; Y. Y. Bai; F. Z. Li; X. Yue; H. Wang; J. Z. Peng; J. Gu, *Nat. Commun.* 2023, ***14***, 5640.

[44] X. Zhu; J. Huang; M. Eikerling, *ACS Catal.* 2021, ***11***, 14521-14532.

[45] Y. Wang; Z. Huang; Y. Lei; J. Wu; Y. Bai; X. Zhao; M. Liu; L. Zhan; S. Tang; X. Zhang; F. Luo; X. Xiong, *Chem Commun (Camb)* 2022, ***58***, 3621-3624.

[46] W. Zheng; J. Yang; H. Chen; Y. Hou; Q. Wang; M. Gu; F. He; Y. Xia; Z. Xia; Z. Li; B. Yang; L. Lei; C. Yuan; Q. He; M. Qiu; X. Feng, *Adv. Funct. Mater.* 2019, ***30***, 1907658.

[47] T. Wang; X. Sang; W. Zheng; B. Yang; S. Yao; C. Lei; Z. Li; Q. He; J. Lu; L. Lei; L. Dai; Y. Hou, *Adv. Mater.* 2020, ***32***, e2002430.

[48] Y. Bao; J. Xiao; Y. Huang; Y. Li; S. Yao; M. Qiu; X. Yang; L. Lei; Z. Li; Y. Hou; G. Wu; B. Yang, *Angew. Chem., Int. Ed.* 2024, ***63***, e202406030.

[49] S. Gong; W. Wang; C. Zhang; M. Zhu; R. Lu; J. Ye; H. Yang; C. Wu; J. Liu; D. Rao; S. Shao; X. Lv, *Adv. Funct. Mater.* 2022, ***32***.

[50] J. Xie; X. Wang; J. Lv; Y. Huang; M. Wu; Y. Wang; J. Yao, *Angew. Chem., Int. Ed.* 2018, ***57***, 16996-17001.

[51] P. Rao; X. Han; H. Sun; F. Wang; Y. Liang; J. Li; D. Wu; X. Shi; Z. Kang; Z. Miao; P. Deng; X. Tian, *Angew. Chem., Int. Ed.* 2024, ***137***, e202415223.

[52] Y. Wang; L. Xu; L. Zhan; P. Yang; S. Tang; M. Liu; X. Zhao; Y. Xiong; Z. Chen; Y. Lei, *Nano Energy* 2022, ***92***, 106780.

[53] S. Yan; C. Peng; C. Yang; Y. Chen; J. Zhang; A. Guan; X. Lv; H. Wang; Z. Wang; T.-K. Sham; Q. Han; G. Zheng, *Angew. Chem., Int. Ed.* 2021, ***133***, 25789-26197.

1

View Article Online
DOI: 10.1039/D6TA00814C

"The data supporting this article have been included as part of the Supplementary Information."

View Article Online
DOI: 10.1039/D6TA00814C